Experiments in Fluids (2006) 41: 559–571
DOI 10.1007/s00348-006-0181-2

RESEARCH ARTICLE

Alexander R. Horner-Devine

Velocity, density and transport measurements in rotating, stratified flows

Received: 15 November 2005 / Revised: 25 April 2006 / Accepted: 13 June 2006 / Published online: 8 August 2006

Abstract A technique is presented for measuring velocity, density and scalar transport in a buoyant rotating gravity current. Existing methods for combined PIV and PLIF are modified for use in a stratified flow on a rotating table and strategies for beam alignment, index of refraction matching, surface tension matching and photobleaching correction are presented. In addition, the PIV–PLIF technique is modified to resolve the velocity and density fields in a cross-section of the current perpendicular to the mean flow direction, allowing the transport in this direction to be computed. This is done by rotating the plane of the laser sheet 15° to the horizontal. This sheet angle is high enough that the entire cross-section of the current is contained in the viewing area, but low enough that horizontal PIV particle displacements are resolved. The technique is used successfully to measure the transport of buoyant fluid in a non-rotating channel to within 5% of the prescribed flow. Results from a rotating gravity current experiment are then presented and compared with previous experiments.

1 Introduction

A number of recent advances in experimental technique have led to powerful methods that combine particle image velocimetry (PIV) and planar laser induced fluorescence (PLIF) to measure velocity and scalar concentration fields simultaneously in fluid flows (Cowen et al. 2001; Borg et al. 2001; Law et al. 2003). The rate of scalar transport, a quantity of considerable importance for environmental flows, can thus be computed in the measurement plane. The PLIF technique is also used in stratified flows in order to measure the density field by initially dyeing different water masses in proportion to their density. In the present work, the PIV–PLIF technique developed by Cowen et al. (2001) is modified for use in stratified geophysical flows.

The goal of the experiments is to measure the velocity, density and transport in a buoyant, wall-bounded gravity current on a rotating table. This flow has been studied extensively in laboratory experiments (Lentz and Helfrich 2002; Avicola and Huq 2002; Griffiths and Hopfinger 1983; Condie and Ivey 1988; Horner-Devine et al. 2006) in order to better understand the dynamics of buoyant coastal currents. In such experiments, buoyant fluid forms a surface-trapped current along a vertical wall in the direction of Kelvin wave propagation. The current is deepest close to the wall, thins to zero thickness at its offshore edge and is typically assumed to be in geostrophic balance (Griffiths 1986). A number of studies have shown that the coastal current may become unstable (Griffiths and Linden 1981; Vinger et al. 1981).

In nature, coastal currents are an important transport mechanism and are known to carry buoyant water and environmentally significant constituents hundreds of miles alongshore. Laboratory experiments that seek to measure the alongshore rate of transport typically measure the mean density field in a plane perpendicular to the flow or the surface velocity field. In the former case, the alongshore velocity must be inferred from the density field, and in the latter case the vertical extent and structure of the velocity and density fields must be inferred from the surface velocity. In both cases the velocity and density fields are assumed to be related according to a geostrophic momentum balance. This assumption may not be valid when viscous dissipation or instability is dynamically significant. Since these may both be important in laboratory models of wall-bounded gravity currents, a better technique is presented.

In order to measure transport in the mean flow direction, velocity and density fields must be resolved in

A. R. Horner-Devine (✉)
Civil and Environmental Engineering,
University of Washington, Seattle, WA, USA
E-mail: arhd@u.washington.edu
Tel.: +1-206-6853032

a vertical plane perpendicular to the mean flow. This is done by rotating the plane of the co-aligned PIV and PLIF laser sheets relative to the horizontal. When the correct angle is chosen, PLIF dye concentrations and along-wall PIV displacements can be resolved simultaneously across the vertical and cross-shore extent of the current, allowing calculation of the alongshore rate of transport. Since the vertical structure of the current is based on a projection from the angled plane of the sheet, the technique is limited to flows for which the scale of alongshore variability is greater than the alongshore extent of the measurement area.

The technique is validated in a series of non-rotating experiments with a known transport rate. Techniques are presented that correct for the effects of index of refraction, photobleaching and variation of surface tension. In further experiments on a rotating table the structure of the current is investigated and is compared with previous rotating gravity current experiments.

2 Experimental setup

All of the experiments were conducted in an annular tank on a 2-m rotating table (Fig. 1). The table, which consists of a circular steel plate attached to a rectangular base by means of a large thrust bearing is level to within 10^{-5}. A servo motor (Pacific Scientific, model R8AG, 50 Nm maximum torque) with a 50:1 orbital gear head (Bayside Motion Group) drives the table with a non-slip drive belt. The motor speed and acceleration are controlled by a PC computer with Galil Motion Control software, in conjunction with a motor controller (Compumotor). This system provides accurate control of the rotation speed and allows very smooth rotation.

The water tank is a 500 l Plexiglas annulus that is 25 cm deep and has 184 and 44 cm diameter outer and inner walls, respectively. The tank is outfitted with a 0.5 cm thick Plexiglas lid to prevent surface stress due to wind shear. A 155 cm high three-legged frame, which straddles the entire tank, supports a high fidelity slip ring and a digital camera mount. The slip ring is used to bring electrical power and a TTL trigger signal onto the table. A second smaller frame is used for on-table electronic components including a image acquisition computer and digital camera controller.

The current is generated along a straight 120 cm Plexiglas interior wall set across one side of the tank. The end section of the wall is hinged so that it makes a right angle with the wall. Buoyant water is introduced into the tank at the level of the water surface through a 5 cm × 1 cm slot by means of a diffuser affixed to the back of the hinged section. The diffuser is a 6.25 cm^3 chamber filled with small plastic beads. Typical flow rates range from 3 to 16 $cm^3\ s^{-1}$ resulting in diffuser residence times less than 1.0 s. The adjustment time for the flow is approximately one rotation period (10–40 s), so the inflow rate can be considered to ramp up instantaneously.

Two experimental configurations are used to generate a buoyant current in a non-rotating and rotating system, respectively. In order to measure the total volume flux, the current must be limited to a width that is less than the field of view in both cases. This is satisfied in the rotating case as the current is held against the wall due to Coriolis acceleration. In order to test the technique in the experimentally simpler non-rotating case, it was necessary to contain the current within a channel. The channel is 5 cm wide and consists of two Plexiglas walls that are installed along the coastal wall in the tank such

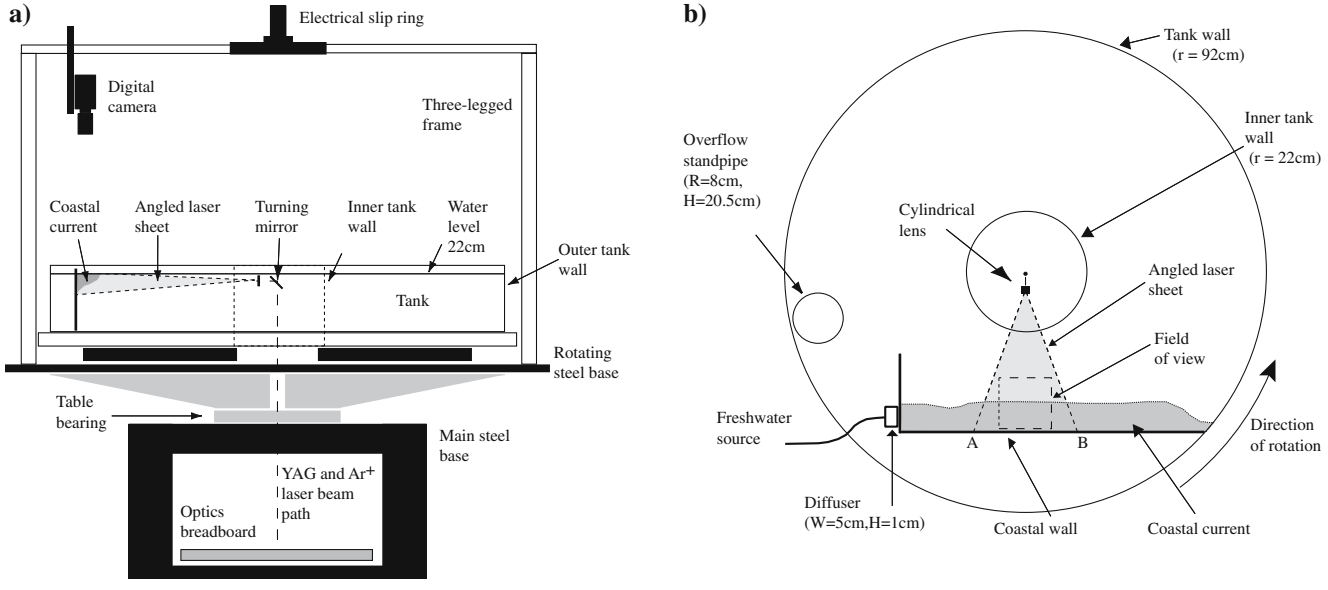

Fig. 1 Schematic of the rotating table viewed from the side **a**, and of the tank configuration viewed from above **b**. The orientation of the angled laser sheet is included in both schematics. In **b** the side of the sheet labeled B extends above the water surface and A extends below the buoyant current

that the non-rotating current occupies approximately the same space as the rotating current. Buoyant water is introduced to both the rotating and non-rotating currents using the source described below. In the non-rotating configuration, the buoyant fluid forms a two-layer flow that is discharged from the channel into the larger tank on the downstream end. The experiment begins after the channel flow has reached steady state.

We measure the flow rate with a ball float flow meter immediately before the flow passes through a slip ring onto the table. The source water is discharged from a constant head system 2.4 m above the rotating table that consists of two 60 l Nalgene tanks. The temperature of the buoyant source and ambient tank water is measured using a 0.01°C resolution thermistor (Fluke Y2039). The temperature in the room is also measured with a ± 0.5°C wall thermometer, since the thermistor picks up noise from the table servo motor when it is enabled and therefore cannot be used during a run. The density is measured with a $\pm 5 \times 10^{-5}$ g cm^{-3} oscillating U-tube density meter (Anton-Paar, model 4500).

PIV and PLIF images are illuminated using a pair of pulsed ND:YAG lasers (120 mJ Gemini PIV, New Wave Laser) and a continuous wave Argon ion laser (5 W Innova 305, Coherent) and imaged with a 30 Hz, 1 k × 1 k, 12 bit CCD camera (SMD1M30_10 Silicon Mountain Designs, now Dalsa Corporation). The lasers are mounted on a large optics breadboard beneath the rotating table (Fig. 2). Beam steering optics and a thin film polarizer on the breadboard are used to focus and co-align all three beams. The co-aligned beams are then directed upward through a 6 mm diameter hole in the center of the table. An angled mirror fixed to the rotating table steers the beams horizontally through a pair of cylindrical lenses to create a light sheet in the rotating frame of reference.

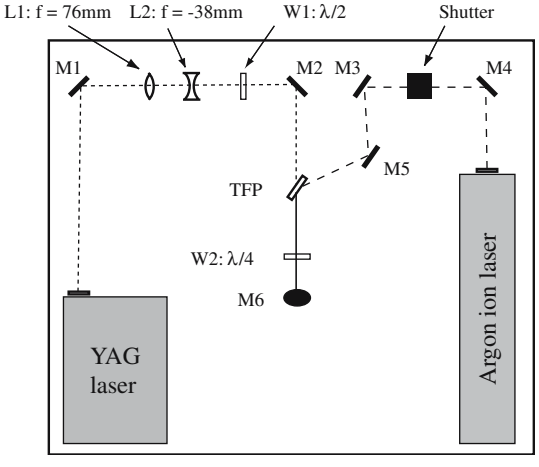

Fig. 2 Schematic of the laser optics (*plan view*). Components are labeled as follows. *M* mirror, *L* lens, *W* waveplate and *TFP* thin film polarizer. Mirror 6 is oriented at 45° to the horizontal so that the beam is directed vertically through the center of the table. The *dashed*, *dotted* and *solid lines* are the Argon ion, YAG and combined beams

3 Measurement technique

In order to calculate the alongshore transport of buoyant fluid in the current, PIV and PLIF are used to measure the velocity and density fields, respectively, in an angled cross-sectional slice of the current.

3.1 Combined velocity and density measurement

Combining PIV and PLIF presents a challenge, since implementation of the former requires that the flow is seeded with particles that reflect light and introduce errors in the measured concentration field. Conversely, emitted light from the PLIF dye can contaminate the PIV images. A number of solutions have been presented to circumvent this problem (Cowen et al. 2001; Borg et al. 2001; Law et al. 2003). The present experiments employ the single camera solution of Cowen et al. (2001). Each snapshot consists of three images, two PIV and one PLIF, which are acquired within 0.1 s. A sharp 514 nm cut-off filter is mounted to the camera to distinguish between the two desired image types. The PIV images are illuminated with the 532 nm ND:YAG lasers. The wavelength of the reflected light from the particles is also 532 nm so it passes through the filter. The PLIF image is illuminated with the Argon ion laser, which has a wavelength of 488 nm. To be successful, the PIV/PLIF technique requires that emitted light from the fluorescent dye passes through the filter, however, light from Argon ion laser reflecting off the particles does not. This is achieved by choosing the appropriate fluorescent dye. Fluorescein is used since its excitation and emission bands are centered at 490 and 530 nm, respectively. There are two known drawbacks to using Fluorescein for PLIF; it can be very sensitive to pH (Walker 1987) and is prone to photobeaching (Crimaldi 1997). Techniques for minimizing errors due to these two effects are presented below.

3.2 Velocity measurement

Implementation of PIV Particle image velocimetry has been used extensively in fluid mechanics experiments to measure fluid velocity. The reader is referred to Raffel et al. (1998) for a thorough introduction to the technique and to Sveen and Cowen (2004) or Liao and Cowen (2005) for a discussion of some recent improvements. Digital PIV involves imaging a cross-section of a particle-seeded flow and then numerically interrogating sequential pairs of images to determine mean particle displacements. The technique uses spatial cross-correlation of sub-windows within the image to determine the displacements from which the velocity is calculated. In this study, second order accurate codes written by Cowen are used to compute particle displacements (Cowen et al. 2001; Cowen and Monismith 1997). The images are

initially interrogated in 64×64 pixel sub-windows. The sub-window size is then decreased iteratively to 32×32 and then 16×16 pixels using the results of the coarser pass to offset the sub-windows at the finer resolution. In addition to decreasing the sub-window size, the width of the weighting function used to account for the correlation bias error was successively decreased on each pass.

Particle seeding In order to accurately measure the velocity in the flow using PIV, it is necessary to have particles dispersed uniformly in the flow. Since the present flow is stratified and since the ambient flow is quiescent, very small particles (Potters Industries, Spherical Hollow Sphere, $\rho_p = 1.1$ g cm^{-3}, $d_p \simeq 11$ μm) were used, which have a fall velocity of 7×10^{-4} cm s^{-1} based on Stokes law. Based on this estimate of the fall velocity, particles are expected to fall approximately 3.6 cm during the 90 min. tank spin-up period. It was sometimes necessary to add particles to the tank during the spin-up in order to ensure that there was adequate coverage, however, we generally did not have trouble keeping enough particles in the images. The particle seeding density was greater than 10^{-6} by mass, which resulted in approximately 20 particles per 32×32 pixel sub-window. This exceeds the minimum desirable count determined by Cowen and Monismith (1997).

Temporal and spatial resolution The timing signal is generated for PIV and PLIF images using a digital delay generator (Berkeley Nucleonics), which has a resolution of 1 ns. The spacing between PIV images is 40 ms and images triples are acquired at 1 Hz. For calibration, an image of a 10×10 cm clear grid is acquired in the plane of the laser sheet. We manually interrogate outer points in the grid image to calculate the dimensional magnification of the optical system, which is $M = 0.013$ cm pixel^{-1}. Further sub-sampling of the image confirmed that the magnification was spatially uniform to within one pixel. Higher accuracy could be achieved by interrogating the grid digitally and solving the over-determined system to compute the mapping for each point independently, as described in Raffel et al. (1998). The current calibration technique is considered to be adequate for resolving the mean flow properties in the current. However, there is no reason that higher accuracy techniques could not be implemented if they were justified. The displacement fields are converted to velocity fields according to

$$(u, v) = \left(\frac{\Delta x M}{\Delta t}, \frac{\Delta y M}{\Delta t}\right).$$

Finally, we filter the velocity fields using a 3×3 median filter to get rid of outliers. The physical width of each image is 13 cm, resulting in a nominal spatial resolution of 0.2 cm. This corresponds to the resolution in the direction perpendicular to the wall. The vertical dimension is obtained by projecting the angled along-wall dimension of the image into a vertical plane. The effective vertical resolution is 0.05 cm.

Index of refraction Optical measurement techniques such as PIV and PLIF are challenging in a stratified fluid because variation in fluid density is usually also associated with variation in index of refraction, n. The variations in n distort the incident laser sheet path resulting in some ambiguity in the sheet location. The path of the light reflected from particles and emitted from the dye is also distorted, resulting in blurring of the image as well as position ambiguity. Both of these significantly decrease the accuracy of PIV and PLIF. Alahyari and Longmire (1994) find that aqueous solutions of glycerol and potassium phosphate could be used to obtain fluid density differences while matching the index of refraction. They show that PIV accuracy improved significantly with matched indices of refraction. We use isopropyl alcohol (rubbing alcohol or 2-propanol) and salt to match n since they are readily available and economical. It has been used successfully for PIV and PLIF experiments by Lowe et al. (2002) and Troy and Koseff (2005). In the range of densities that are relevant to this study, the variation of n with density is approximately linear and given by,

$$n_a = 1.9802 - 0.6499\rho_a, \quad (1)$$
$$n_s = 1.0924 - 0.2411\rho_s, \quad (2)$$

for alcohol and salt solutions (Fig. 3). Each density difference, therefore, corresponds to a single index of refraction.

For a desired $\Delta\rho = \rho_s - \rho_a$, ρ_s and ρ_a are chosen so that n is matched. Rearranging Equations 1 and 2, the matched index of refraction n_m is expressed in terms of $\frac{\Delta\rho}{\rho_s}$ as

$$n_m = \frac{4.5313\frac{\Delta\rho}{\rho_s} - 7.5782}{4.1479\frac{\Delta\rho}{\rho_s} - 5.6867} \quad (3)$$

A potential drawback of using isopropyl alcohol for index of refraction matching is that alcohol has a higher viscosity than water. For the majority of runs we use 1.8% alcohol, corresponding to an increase in the viscosity of the solution of less than 10%.

Surface tension Adding alcohol to the source water also reduces the surface tension of the fluid. The surface tension of pure isopropyl alcohol is 20.93 dyn cm^{-1} compared with 71.99 dyn cm^{-1} for pure water. This difference drives a surface flow when the alcohol–water solution from the source comes in contact with the ambient salt water. The source water moves radially away from the source across the surface of the water immediately after the source is turned on. The spreading is eventually arrested due to friction, leaving a thin buoyant layer that extends offshore well beyond the edge of the buoyant current. This layer is eventually accelerated by Coriolis and forms a distinct current. Since the current induced by the surface tension difference draws both mass and momentum from the primary current, it causes noticeable deviations in the dynamical description of the flow.

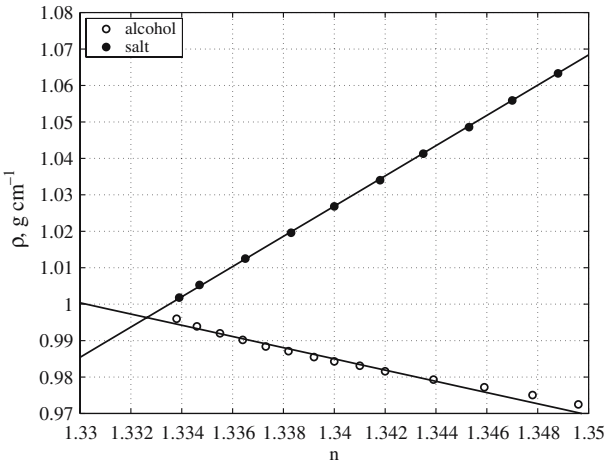

Fig. 3 Variation of density with index of refraction for isopropyl alcohol (2-propanol) and salt (sodium chloride). The *lines* represent linear regressions to the first 12 points. Data are from Lide (2003)

In order to avoid this source of error, a small amount (25 ml) of strong commercial surfactant (Kodak Photo-Flo 200) is added to the tank prior to the run. We determined the appropriate concentration of surfactant by incrementally increasing the concentration in a sample container of ambient tank water until a drop of source fluid released on the surface no longer induced a pronounced surface flow. We adjust the concentration of surfactant for runs with different g' and thus different alcohol concentration.

3.3 Density measurement

Implementation of PLIF Planar laser induced fluorescence is used to measure the density field in the flow. The technique involves illuminating the desired field of view with a thin laser sheet and adding a known concentration of fluorescing dye to the buoyant source water. The dye and laser combination is chosen so that the dye (in our case fluorescein) is optimally excited at the wavelength of the illuminating laser light (in our case 488 nm from the Argon ion laser). When it is excited, the dye emits light at a higher wavelength and its intensity is proportional to both the incident laser light intensity and the local dye concentration. The distribution and intensity of emitted light in the laser sheet is measured with the CCD chip in the digital camera. After properly correcting for the distribution of incident laser intensity, the intensity in the acquired PLIF images is correlated with the dye concentration. Thus, high intensity regions in the image correspond to regions in the flow with high dye concentration. Since dye is added to the buoyant inflowing fluid in a known amount, the fluid density can subsequently be computed from the dye concentration field. Below we describe the implementation, corrections, and calibration of PLIF that were used for the present experiments.

In order to calculate the dye concentration, $C_n(i,j)$, from the acquired digital images, we follow the method described in Crimaldi and Koseff (2001). Here the pixel indices are $1 < i < 1{,}024$ and $1 < j < 1{,}024$, and n is the image index. In this method, variations in dye fluorescence, laser sheet intensity, and pixel response in the acquired digital image $A_n(i,j)$ are accounted for using a background image $B_n(i,j)$ with a low, spatially uniform dye concentration and a dark response image $D(i,j)$. The effectiveness of the background image correction technique relies on the assumption that the chemical properties of the water, the laser sheet illumination, and the pixel response are identical in $A_n(i,j)$ and $B_n(i,j)$. Assuming that this is true, the corrected image $A'_n(i,j)$ is computed according to

$$A\prime_n(i,j) = \frac{A_n(i,j) - B_n(i,j)}{B_n(i,j) - D(i,j)}. \tag{4}$$

For each experiment, the dark response image $D(i,j)$ is obtained by averaging 50 images immediately after the experiment in a completely darkened room with the lens cap on. Acquiring the background image is more involved since very small variations in the optical alignment result in illumination that varies as the table is rotated. This requires that a separate background image is acquired for each PLIF image in the experiment. These background images are acquired before each experiment using the same timing and illumination, but with only a low, uniform concentration of Fluorescein in the tank.

For the present experiments, the background dye concentration is not easily measured, therefore, the concentration is calibrated relative to the undiluted dye concentration of the source water. The ambient dye concentration is very small relative to the source concentration and is assumed to be zero for the purposes of calibration. A separate image of undiluted source water, A_{src}, is acquired prior to the run for the calibration. A corresponding background image is also acquired and A_{src} is processed using Eq. 4. The average intensity is found in the region of the corrected image A'_{src} that corresponds to the undiluted source water so that we have a scalar representing the maximum concentration. In practice, three methods are used to measure the scalar intensity of the undiluted source fluid, a_{src}, based on spatial averaging of the corrected image A'_{src}. In the first method, source fluid is discharged through a 2 mm diameter nozzle forming a jet in the plane of the laser sheet. Ten images of the jet are averaged and corrected as above. The scalar intensity corresponding to the source water, a_{src}, is the average intensity in the 10×10 pixel region corresponding to the potential core of the jet. In the second method, a $26 \times 11 \times 9$ cm Plexiglas box is filled with source fluid and placed in the laser sheet so that it is illuminated through the long side. A composite average image is generated from ten images and corrected for attenuation (see Sect. 3.3.1). The composite image is further averaged

across the image to obtain a single intensity profile. The scalar intensity corresponding to the source water, a_{src}, is the maximum intensity in the averaged profile (Fig. 4). In the third method, the maximum pixel intensity in a uniform flow in the rectangular test channel is used. This value is obtained by averaging the intensity in the region of unmixed fluid in the buoyant surface layer. Although all three methods resulted in comparable values for the source intensity, the third generated the most consistent calibration.

If we assume that the background concentration, the background image, and the dark response are the same in the source images as in the images taken during the run, we can normalize the run images by the maximum concentration in the source image, a'_{src}, and obtain the scaled dye concentration

$$\frac{C(i,j)}{C_{\mathrm{o}}} = \frac{A(i,j)\prime}{a\prime_{\mathrm{src}}}.$$

Finally, the density anomaly is obtained from the scaled concentration field according to

$$\rho(i,j) = \rho_{\mathrm{a}} - \frac{C(i,j)}{C_{\mathrm{o}}}\rho_{\mathrm{s}},$$

where ρ_{a} and ρ_{s} are the ambient and source fluid densities, respectively. When calculating the transport of buoyant fluid, the scaled concentration $\frac{C(i,j)}{C_{\mathrm{o}}}$ is used directly to represent the scaled buoyancy anomaly $(\rho_{\mathrm{a}} - \rho)/\rho_{\mathrm{s}}$.

3.3.1 Attenuation

The intensity of laser light is attenuated in proportion to the concentration of dye and PIV particles present. Attenuation due to water alone and background concentrations of dye and particles is accounted for with the background correction described above. When buoyant water is present, however, the attenuation depends on the instantaneous distribution of dye and particles in the image. Dye concentration in the image is under-predicted as a result of the decrease in the local laser sheet intensity caused by attenuation. Cowen et al. (2001) describe this problem and establish a solution technique that is the basis of the correction used in the present work. The interested reader is referred to their paper for a complete description of the theory and validation of the technique.

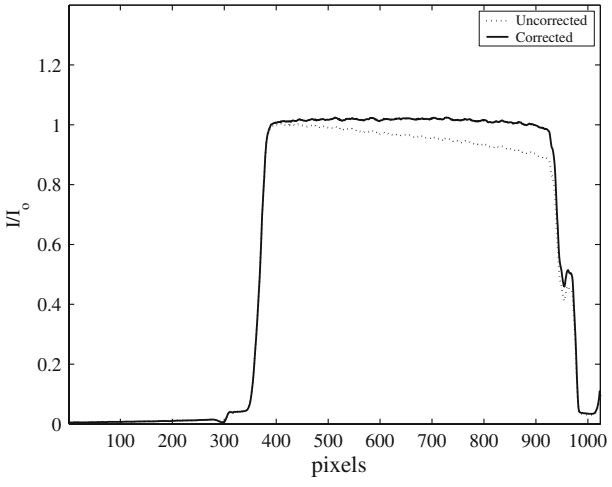

Fig. 4 Normalized intensity in a box of source fluid with and without correction for attenuation. I_o is the maximum intensity in the raw profile. The walls of the box are 350 and 930 pixels from the left side of the image

In order to correct for the variation in laser intensity, the attenuation must be estimated at each point in the sheet. Following Cowen et al. (2001), an effective attenuation coefficient η_{eff} is determined that accounts for dye and particles together. The coefficient is estimated based on the source box intensity profile (Fig. 4) according to

$$\eta_{\mathrm{eff}} = -\frac{1}{x_2 - x_1}\log\left(\frac{I_2}{I_1}\right),$$

where (x_1,I_1) and (x_2,I_2) are points in the linearly decreasing section of the profile between 400 and 900 pixels. The true concentration at each point depends on the concentration along the path after it has been corrected for attenuation and so the correction must be applied recursively. The attenuation is calculated progressively along the beam path and the concentration is corrected for attenuation at each step before the attenuation is calculated for the next point along the beam path. Finally, the concentration is corrected based on the new value for the laser intensity at each point.

In the above technique, the attenuation coefficient is measured using sample fluid that includes dye and particles so that, while only dye concentration is measured in the images, both are included in calculating the laser attenuation. An assumption has been made, therefore, that the mixing rates of the dye and particles are similar. This assumption has not been tested explicitly in the present work. However, the success of the technique for measuring transport indicates that it is reasonable.

3.3.2 pH compensation

The efficiency with which dissolved fluorescein emits light is known to be a strong function of the pH of the solution (Walker 1987). The variation in emission with pH is greatest in the range between pH = 6 and 8, with low emission for solutions with pH < 6. For pH > 8, emission is maximized and is effectively independent of pH. In order to avoid the effects of pH, therefore, we buffer both the tank and source water using sodium carbonate (Na_2CO_3) to greater than pH = 8.5 for each run.

3.3.3 Surface location

Image-based experiments in near-surface flows present an additional challenge since the exact location of the

surface must be determined in the image. This is complicated in the present experiments since the angled laser sheet reflects off the surface and illuminates regions of the image that are not in the desired flow cross-section. Accurate location of the surface is necessary for computing the transport in the image cross-section. Two techniques were compared for determining the surface location. In the first, a series of PIV images were averaged. Since a few buoyant particles inevitably collect on the water surface, a clear band of higher intensity pixels corresponding to these particles is evident in the images. The surface location is taken to be the location of maximum intensity in the average, smoothed intensity profile. The second technique identifies the surface in a similar fashion in the PLIF image. Both techniques provided similar results. The standard deviation of the surface location was 16 pixels over the course of one experiment based on the PLIF technique. Since the sheet is inclined, this corresponds to 0.05 cm in the vertical and an error in the transport measurements of less than 5%. For the purposes of the transport calculations, an average value of the surface location was used.

3.4 Angled sheet

In order to capture the entire cross-section of the current, the YAG and Ar^+ laser sheets are angled relative to horizontal. To generate each sheet, laser light is directed outward from the center of the table through a cylindrical lens. The axis of the sheet is horizontal and perpendicular to the coastal wall and flow direction (Fig. 1). The sheet is rotated about its axis such that the upstream edge is below the current and the downstream edge is above it. The camera is rotated by approximately the same amount as the sheet. The camera angle is fine-tuned with the illuminated grid plate in place to ensure that the entire field of view is in focus.

Since the sheet has a finite thickness ($\sim$ 1.5 mm), particles that are displaced horizontally by a small amount stay in the sheet and have a measurable displacement in the angled plane of the sheet (Fig. 5). Errors in the measured along-shore velocity are minimized when the sheet angle θ_s is small.

The actual horizontal displacement, Δx, is mapped into the viewing plane, Δs, according to $\Delta s = \Delta x \cos\theta_s$. The in-sheet displacements are converted to actual displacements by inverting this relationship,

$$\Delta x = \frac{\Delta s}{\cos\theta_s}.$$

It is important to note that the technique cannot differentiate between vertical and horizontal velocities. However, a low sheet angle reduces the contribution to the measured displacement, $\Delta s'$, by a vertical displacement, Δz according to

$$\Delta s\prime = \Delta z \sin\theta_s.$$

The error in Δs due to a vertical displacement is given by

$$\frac{\Delta s\prime}{\Delta s} = \frac{\Delta z}{\Delta x}\tan\theta_s.$$

According to the continuity equation $\Delta z/\Delta x \sim h/L$. For the rotating gravity current, a conservative estimate of the representative length scale, L, in the coastal current is the Rossby radius, $L_r = (g\prime h)/f$, where $g\prime = g\Delta\rho/\rho$, f is the Coriolis frequency and h is the local current depth. For typical flow parameters, h = 1 cm and L_r = 5.3 cm. This gives an estimate for the error due to velocity ambiguity of 5%.

A vertical cross-section of the current is obtained by projecting the resolved velocity field from the angled sheet onto a vertical plane, where the vertical coordinate is given by $z = s\ \sin\theta_s$. The projected cross-section accurately describes a vertical section of the current if the scale of along-wall variability in the current is much greater than the length of the measurement area, $s\ \cos\theta_s$ = 12.6 cm. Near the gravity current head the scale of variability is expected to be on the order of the Rossby radius. Thus the projected section will not be representative of a vertical section. Far from the head of the current, however, the scale is expected to be much longer and the projected vertical section will be accurate.

3.4.1 Photobleaching

Fluorescein dye is known to be susceptible to photobleaching, whereby the emission efficiency of dye molecules depends on the duration of exposure to laser light Crimaldi (1997). Photobleaching introduces errors into the concentration measurements since emission from the dye depends on its residence time in the laser sheet and thus the velocity. Crimaldi (1997) showed that the fluorescence, F, at a single point normalized by the unbleached fluorescence, F_o, is

$$\frac{F}{F_o} = \left(\frac{2}{\pi}\right)^{3/2}\exp(-B_{pb}),$$

where B_{pb} is a photobleaching parameter given by

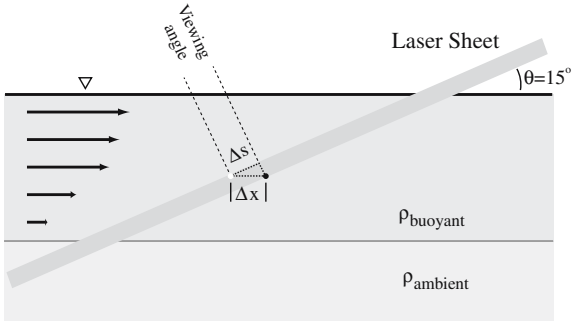

Fig. 5 Displacement schematic for the angled slice technique. View from the coastal wall side

$$B_{\mathrm{pb}} = \frac{PQ_{\mathrm{b}}\sigma}{(2\pi)^{1/2}ahvU}.$$

In the above expression, P is the laser power, Q_{b} is the quantum bleaching efficiency, σ is the absorption cross-section, $2a$ is the e^{-2} beam width, h is Planck's constant, v is the frequency of the laser light and U is the fluid velocity. Higher values of B_{pb} result in more photobleaching and greater error on the fluorescence.

Crimaldi (1997) provides a numerically integrated solution for the fluorescence in a measuring volume, which is appropriate for a laser sheet with finite width. Since B_{pb} is an inverse function of velocity, the fluorescence, and therefore the concentration, will be under predicted in regions of the current where velocity is low. It is important to note that errors in concentration measurement in slow regions of the current contribute relatively small errors to the totally flux measurement. Nonetheless, because we know the velocity at each point in the density field, we can estimate and correct for the errors due to photobleaching. In order to make the correction computationally tractable, we estimate the numerically integrated function used by Crimaldi as

$$\frac{F}{F_{\mathrm{o}}} = \exp(-B_{\mathrm{pb}}/2). \tag{5}$$

The fluorescence decreases rapidly for $0.01 < B_{\mathrm{pb}} < 10$ (Fig. 6).

In our case, $P = 1$ W (where we have accounted for losses in the optics system), $Q_{\mathrm{b}}\,\sigma = 2.8 \times 10^{-24}$ m^2 (as reported by Crimaldi (1997) for fluorescein), $a = 7.5 \times 10^{-4}$ m, $h = 6.621 \times 10^{-34}$ Js, $v = 6.1475 \times 10^{14}$ s^{-1} and $U \cong 1$ cm s^{-1}. This gives a value of $B_{\mathrm{pb}} = 0.37$, for which $F/F_{\mathrm{o}} = 0.83$. Since much of the plume will have $U < 1$ cm s^{-1}, the local error in the uncorrected concentration field due to photobleaching will be at least 17% is these slow regions.

In order to correct the entire concentration field, the computed velocity field $U(i,j)$ is used to calculate an array of $B_{\mathrm{pb}}(i,j)$ values corresponding to each point in $A(i,j)$. The reduction in fluorescence, F/F_{o} at each point is then calculated according to Eq. 5. Finally, the corrected concentrations are calculated according to

$$A_{\mathrm{corrected}} = \frac{A}{F/F_{\mathrm{o}}}$$

The correction algorithm has difficulty in regions outside the plume where $U(i,j) \rightarrow 0$, and therefore $B_{\mathrm{pb}} \rightarrow \infty$ and $F/F_{\mathrm{o}} \rightarrow 0$. If there is a trace amount of dye above the background level, then the corrected concentration will be very high. In order to avoid this, we set $F/F_{\mathrm{o}} = 1$ for regions of the image where $U < 0.05$ cm s^{-1}. Since the cut-off velocity is very small, however, this correction does not influence the total flux significantly. The error in the computed buoyant transport due to photobleaching was found to be approximately 4%.

Because of the cut-off that must be imposed for very low velocity regions of the flow, this correction may generate artifacts in such regions. While these do not significantly affect the flux calculations, they do alter the observed structure of the flow slightly. A better solution for such low velocity regions would improve this technique.

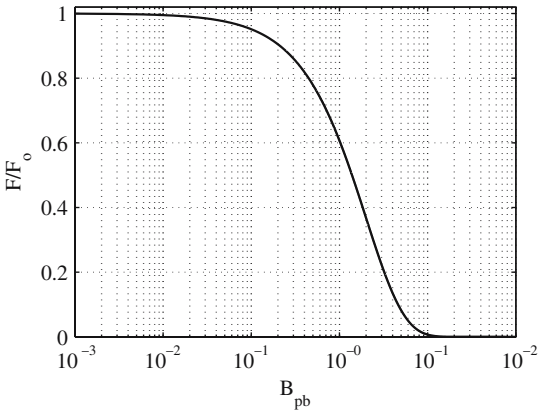

Fig. 6 Estimate of the decrease in fluorescence due to photobleaching as expressed by Eq. 5

4 Results

Two sets of experiments are described: non-rotating validation experiments and rotating experiments. As described in Sect. 2, the non-rotating experiments employed a Plexiglas channel, which was installed along the wall in the tank so that the current could not expand laterally. After it was initiated, the flow was maintained until a steady two-layer flow was achieved in the channel. This was repeated for three different flow rates so that the measured transport of buoyant fluid in the current could be compared to a known inflow. For the rotating experiments, the channel was removed but the inflow was still directed along the wall. For each of these experiments, the table was rotated for more than 90 min before the initiation of the current so that the ambient fluid approached solid body rotation. Four experiments were conducted, including two inflow rates and two density anomalies.

4.1 Non-rotating validation experiments

The goal of this set of experiments is to confirm that the technique accurately measures the transport of buoyant fluid. Non-rotating experiments were chosen to simplify the system and to avoid potential errors associated with calibration of the background intensity when the table is rotating. The calibration is tested for the rotating case in the subsequent set of experiments.

Instantaneous concentration and velocity fields after the current has achieved steady state are shown in Fig. 7. The fluid in the lower layer is nearly stationary and the interface between the two fluids is thin. The

transport of buoyant fluid is calculated from the velocity and concentration fields according to

$$Q_{\mathrm{fw}} = \int\int \frac{C(y,z)}{C_{\mathrm{o}}} u(y,z)\mathrm{d}y\mathrm{d}z \tag{6}$$

where C and C_{o} are the local and inflow dye concentrations, respectively, and u is the along-channel velocity. We integrate over the whole cross-section of the channel in y and z, the across-channel and vertical coordinates.

In Fig. 8 the measured transport is normalized by the inflow rate for three different flow rates, 6.4, 9.8 and 13.2 ml s^{-1}. In all three cases, the transport is still approaching steady state at the beginning of the measurement period. All three measured rates are within 5% of the inflow discharge once steady state is achieved.

4.2 Rotating experiments

Four experiments are carried out with the table rotating. Since the inflow is parallel to the wall, the transport at the measurement location is equal to the source discharge. For these experiments, the inflow geometry and discharge Q are fixed and the table rotation period T and reduced gravity $g' = g\Delta\rho/\rho$ are varied (Table 1). The temporal and spatial resolution of the present data is considerably higher than any previous laboratory coastal current study. However, the experiments only span a small range of the Rossby and Froude number parameter ranges. Here we define the Rossby and Froude numbers based on inflow parameters as $\mathrm{Ro} = QT(4\pi H)^{-1}W^{-2}$ and $\mathrm{Fr} = Q\,W^{-1}\,g'^{-1/2}H^{-3/2}$.

When the table is rotating, the current is held to the wall due to Coriolis acceleration and is expected to be in cross-shore geostrophic momentum balance. The projected concentration and velocity fields are shown in Fig. 9 for a cross-section of the current (Run 2 in Table 1).

The measured buoyancy and velocity fields from Run 2 are shown in Fig. 9a and b, respectively. Both fields represent averages over 3.3 rotation periods. The buoyancy field has been corrected using the background and attenuation corrections outlined in Sect. 3.3. These images have not been corrected using the photobleaching correction for the reasons outlined in Sect. 3.4. In order to compare the two fields directly without loosing any of the resolution in the buoyancy field, the velocity data were interpolated onto the same 1,024 by 1,024 grid as the PLIF image.

A wall-bounded buoyant current in a rotating system is expected to adjust until its momentum in the direction perpendicular to the wall is geostrophically balanced (Griffiths 1986). The predicted along-wall geostrophic velocity is calculated from the density field as

$$u_g = -\frac{g}{f}\frac{\partial}{\partial y}\int_{-z}^{0}\frac{\Delta\rho}{\rho_o}\mathrm{d}z. \tag{7}$$

The geostrophic velocity corresponding to the density field in Fig. 9a is shown in Fig. 9c. Qualitatively, it is nearly identical to the measured velocity field in Fig. 9b. The difference between the two is less than 5% of the maximum velocity in the current (Fig. 9d). The reason for the high ageostrophic velocity observed below the current is unclear and is the subject of further investigation. Within the current, the difference is greatest near the edges where ageostrophic motion is expected due to the wall, surface and interfacial stresses. The maximum error in the three other runs is approximately 10%, and is also focused primarily in the boundary layer regions.

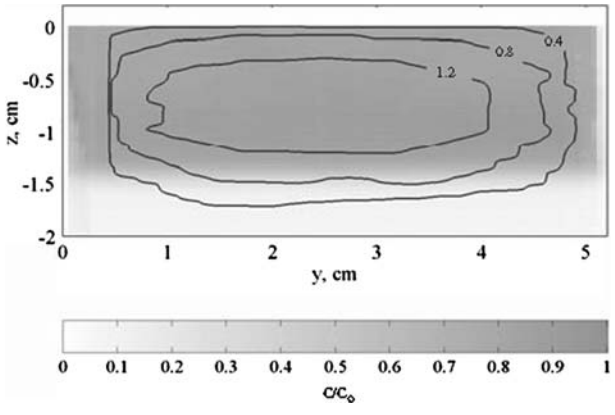

Fig. 7 Instantaneous velocity (*line contours*) and concentration (*color contours*) in a non-rotating channel cross-section. Velocity contours are given in cm s^{-1}

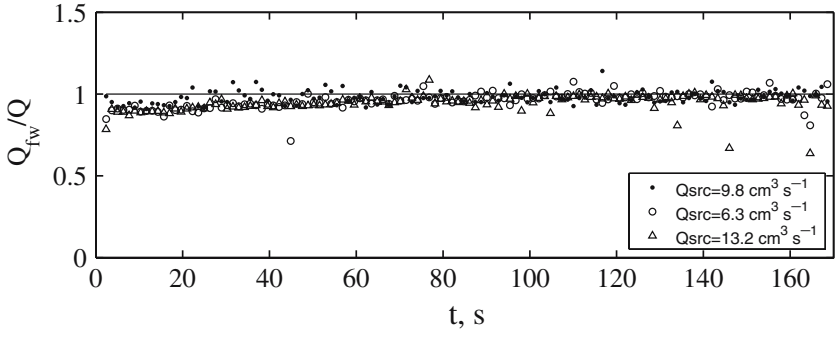

Fig. 8 Freshwater flux in the non-rotating channel calculated according to Eq. 6 for three inflow rates

Table 1 Experimental parameters for rotating gravity current runs

Run	T (s)	Q ($cm^3 s^{-1}$)	g' (cm s^{-2})	W (cm)	H (cm)	Ro	Fr
1	25	9.8	7	5	1	0.78	0.74
2	20	9.8	7	5	1	0.62	0.74
3	25	9.8	3.5	5	1	0.78	1.00
4	20	9.8	3.5	5	1	0.62	1.00

This suggests that the measured velocity field in the angled slice agrees with the expected velocity field to a very high degree.

We define the interface as the location of maximum vertical density gradient. The interface is roughly linear beneath the core of the current and becomes horizontal in the regions close to the wall and at the edge of the plume. On the offshore edge of the current the buoyant layer extends away from the main flow in a thin viscous surface layer.

The current depth at the wall, h_o, is 1.25 cm. Based on this value, the propagation speed and width are expected to scale with $c_i = (g' h_o)^{1/2} = 3$ cm s^{-1} and $L_r = (g' h_o)^{1/2}/f = 4.7$ cm. A cross-shore profile of near-surface velocity illustrates the width based on the maximum velocity gradient as well as the location of maximum velocity (Fig. 10a). In this case, the point of maximum shear, $y_s = 6.5$ cm ($1.4\ L_r$), the point of maximum velocity $y_v = 4.4$ cm ($0.93 L_r$) and the maximum velocity is 2.2 cm s^{-1} ($0.73 c_i$).

Because of the thin surface layer, it is not feasible to determine the edge of the current based on the outer edge of the density field for the whole run. For comparison with previous dye experiments, however, we average the density field vertically to simulate the integrated view of a dyed current and define the edge of the plume, $y_{2\rho}$, as the point where the second derivative of the integrated buoyancy is greatest (Fig. 10b). Using this definition, we obtain a current width of 6.4 cm ($1.4 L_r$).

Current width As stated above, the current width is expected to scale with the Rossby radius, and thus the current depth. The current depth, h_o, deepens over the course of the run until it approaches a constant value after approximately 2–4 rotation periods for all four

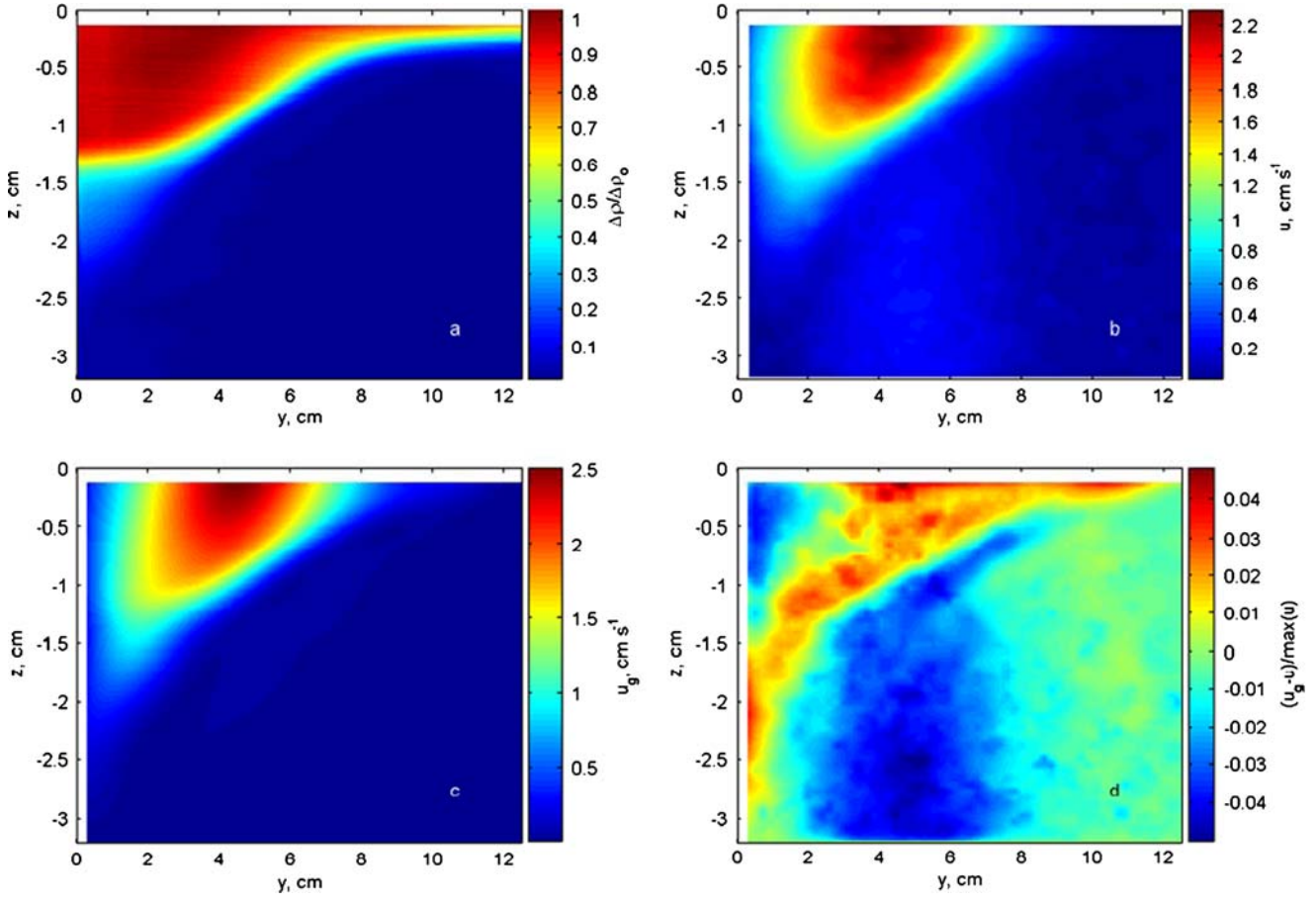

Fig. 9 Cross-shore section of the coastal current buoyancy and velocity fields from Run 2 averaged over approximately three rotation periods. **a** Measured buoyancy normalized by the inflow buoyancy. **b** Measured velocity interpolated onto the finer LIF grid. **c** Geostrophic velocity computed from the buoyancy field. **d** Ageostrophic velocity, computed from the measured velocity field and the computed buoyancy field, normalized by the maximum measured velocity. The maximum deviation from geostrophy is 5%

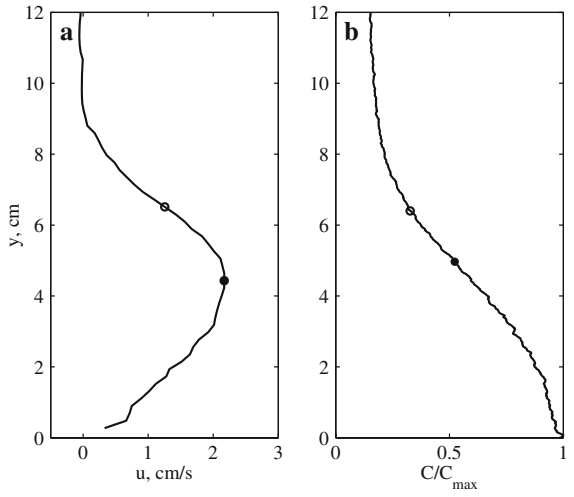

Fig. 10 Cross-shore profiles of surface velocity (**a**) and depth averaged buoyancy (**b**). The *solid* and *open circles* in **a** mark the location of maximum velocity and shear. The *solid* and *open circles* in **b** mark the location of maximum first and second derivatives in the integrated buoyancy. The buoyancy has been normalized by the local maximum for plotting

runs (Fig. 11). The higher g' runs reach the steady depth earlier than the lower g' runs, presumably because c_i is higher and thus information propagates more quickly. We define a steady depth, $\overline{h_o}$, for each run as the average value between 4 and 7 rotation periods and compute a corresponding Rossby radius, $\overline{L_r}$, and gravity current propagation speed, $\overline{c_i}$. The current width, as measured by either y_s or $y_{2\rho}$ and normalized by the steady Rossby radius, widens during the first four rotation periods and then levels off to a constant value (Figs. 12, 13). The average value of the steady width is $(1.23 \pm 0.14)\overline{L_r}$ and $(1.28 \pm 0.13)\overline{L_r}$ for y_s and $y_{2\rho}$, respectively. This value for y_s is much greater than the value of $0.42\overline{L_r}$ measured by Stern et al. (1982). We expect that this is because they were only able to measure the current width close to the nose of the current and thus did not measure the equilibrium width. The value that we obtain for the current width, $y_{2\rho}$, agrees well with the Griffiths and Hopfinger (1983) value of $1.4\overline{L_r}$. Since we calculate the width based on curvature in the vertically averaged density profile, it is not surprising that our value is slightly lower than theirs, which is based on the maximum offshore extent of the dye.

Current stability Both y_s and $y_{2\rho}$ increase smoothly during the first four rotation periods for all four runs. For later time, however, the variability increases noticeably for both of the lower g' runs (Figs. 12, 13; grey circles). This is probably indicative of instability along the front. Four rotation periods corresponds with the time when the current has widened to approximately $y = \overline{L_r}$. This is consistent with Griffiths and Linden (1981), who found that the unstable current width was a function of $\overline{L_r}$.

Current speed When the nose of the current first arrives in the measurement section ($1 < t/T < 2$), the maximum velocity is equal to $\overline{c_i}$ (Fig. 14). Subsequently, the maximum speed decays exponentially and is relatively constant after four rotation periods. The average value of the steady velocity maximum is $(0.74 \pm 0.09)c_i$.

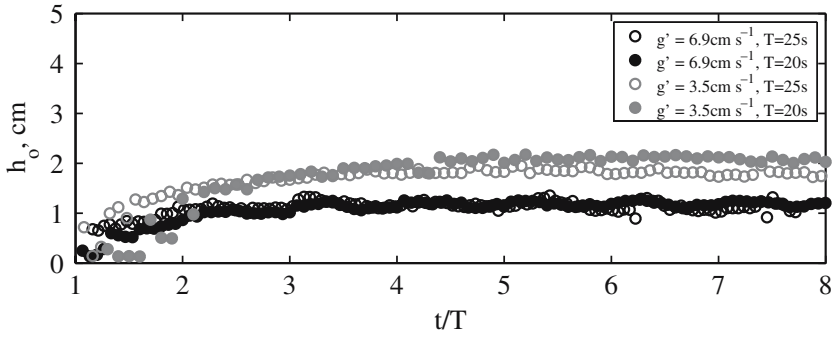

Fig. 11 Coastal current depth at the wall, h_o for all four runs

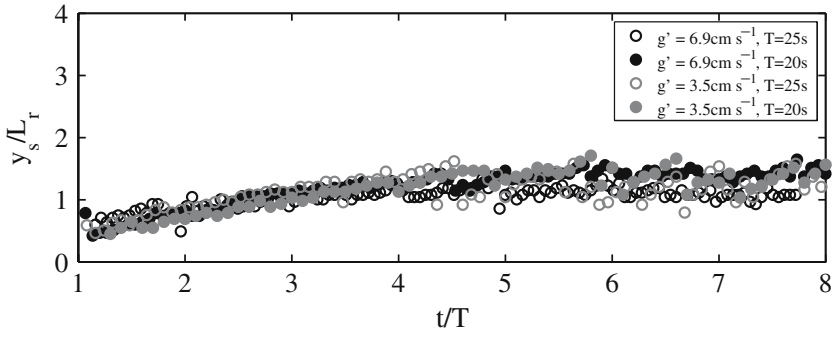

Fig. 12 Location of maximum shear normalized by the Rossby radius in the coastal current for all four runs

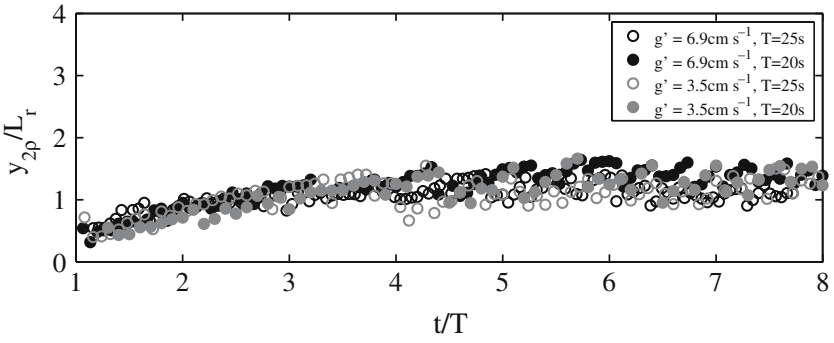

Fig. 13 Location of the offshore plume front normalized by the Rossby radius in the coastal current for all four runs. The front is defined as the maximum in the second derivative of the vertically averaged buoyancy

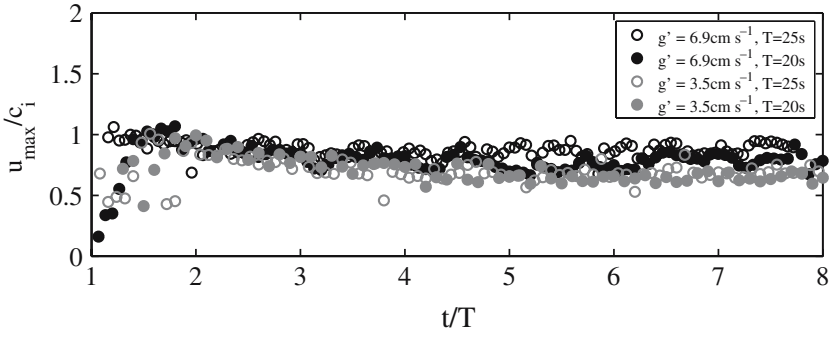

Fig. 14 Maximum velocity normalized by the propagation speed in the coastal current for all four runs

Lentz and Helfrich (2002), Griffiths and Hopfinger (1983) and Stern et al. (1982) all observe a decay in the nose speed and an increase in the current width. Lentz and Helfrich (2002) show that the nose speed decays as $t^{-1/2}$ and the current width increases as $t^{1/2}$, which is consistent with the observations in the two other studies. They hypothesize that the temporal evolution of the current is due to viscous interfacial drag between the buoyant current and the ambient fluid. The $t^{-1/2}$ and $t^{1/2}$ dependence for the velocity and width of the current qualitatively describes the evolution that we observe in the first 1–4 rotations periods. However, the width and speed appear to be steady after that. This indicates that, while interfacial drag and offshore Ekman transport continue to be important, the coastal current may achieve a cross-shore balance.

Transport Finally, since we can calculate the transport directly, it is useful to compare it to the scaling for geostrophic transport, $Q_g = (g\prime h_o^2)/2f$ (Fong and Geyer 2002; Lentz and Helfrich 2002). The transport of buoyant water is calculated in the same fashion as for the non-rotating experiments. The data are filtered with a Butterworth filter that has a filter width equal to the rotation period. Q_g is a reasonably good estimate of the along-shore transport of buoyant fluid (Fig. 15). Note that in our experiments, the measurement location is 54 cm downstream of the source and so the transport at that location will be subject to a lag due to the advective travel time of the current. The estimate is very sensitive to the depth, h_o. The depth measurement depends on the location of the water surface in the image, which can be a somewhat noisy measurement. We expect that this error explains the variation in the transport estimates.

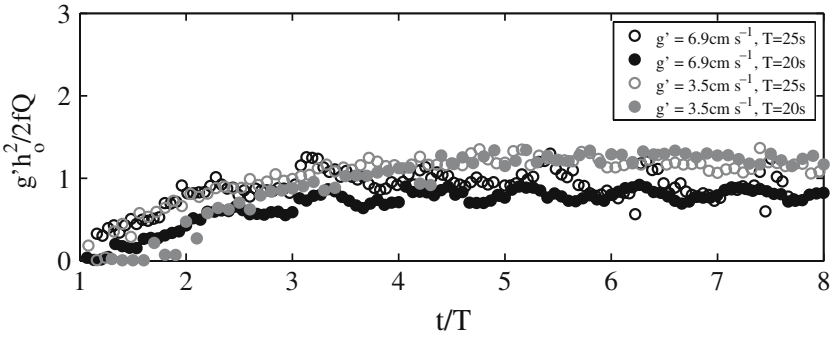

Fig. 15 Normalized geostrophic estimate of alongshore transport $(g\prime h_o^2/2f)$

5 Conclusions

Velocity and density are measured simultaneously in the cross-section of a rotating buoyant gravity current using PIV–PLIF. The implementation of the PIV–PLIF technique described in the current work involves two new modifications. The first is to adapt the existing technique for use on a rotating table. The second modification allows the transport in a buoyant current to be measured directly. This involves rotating the measurement plane 15° from the horizontal so that the entire cross-section is captured, but particle displacements are still resolved. The two acquired fields are used to calculate the instantaneous transport of buoyant fluid through the cross-section. The technique is successful in measuring the transport in a non-rotating channel to within 5% of the prescribed flow rate.

The measurement technique is subsequently applied to a buoyant rotating gravity current. After the current arrives at the measurement area, it is observed to deepen, widen and slow for 1–3 rotation periods and then level off to a constant depth, width and speed for the remaining 4 rotation periods of the run. A gravity current propagation speed, $\overline{c_i}$, and a Rossby radius, $\overline{L_r}$, are defined based on the steady depth achieved at the end of the run. The maximum velocity in the current is equal to $\overline{c_i}$ near the nose and decays to a steady value of $0.74 \pm 0.09\overline{c_i}$. The steady widths of the current, measured according to the location of maximum velocity shear and the offshore inflection point in the density profile, are $1.23 \pm 0.14\overline{L_r}$ and $1.28 \pm 0.13\overline{L_r}$, respectively. These agree with the width reported by Griffiths and Hopfinger (1983). The geostrophic scaling, $Q_{\mathrm{fw}} = (g'h_o^2)/2f$, is relatively successful at predicting the transport in the coastal current, but may be sensitive to errors associated with determining the current depth exactly.

Direct calculation of the geostrophic velocity field using the measured density field agrees with the measured velocity field to within 5–10%. Furthermore, the observed deviations from geostrophy are concentrated near the edges of the current, where viscous diffusion of momentum is expected to be significant. This agreement, in addition to the results in the non-rotating channel, confirm that the technique is accurate and capable of high resolution measurement.

It is important to note that the angled slice technique is expected to be susceptible to significant out-of-plane errors in highly turbulent or three dimensional flows. The limits of its applicability have not been tested here, but it is expected to yield accurate results for a broad class of laboratory flows.

Acknowledgments The author would like to thank M. Brennan for suggesting the angled laser sheet, and S. Monismith, D. Fong, C. Troy, E. Cowen and J. Crimaldi for support in the development and implementation of the experiments. This research was supported by NSF grant OCE-0118029.

References

Alahyari A, Longmire E (1994) Particle image velocimetry in a variable-density flow: application to a dynamically evolving microburst. Exp Fluids 17(6):434–440

Avicola G, Huq P (2002) Scaling analysis for the interaction between a buoyant coastal current and the continental shelf: experiments and observations. J Phys Oceanogr 32(11):3233–3248

Borg A, Bolinder J, Fuchs L (2001) Simultaneous velocity and concentration measurements in the near field of a turbulent low-pressure jet by digital particle inmage velocimetry-planar laser-induced fluorescence. Exp Fluids 31:140–152

Condie S, Ivey G (1988) Convectively driven coastal currents in a rotating basin. J Mar Res 46(3):473–494

Cowen E, Monismith S (1997) A hybrid digital particle tracking velocimetry technique. Exp Fluids 22(3):199–211

Cowen E, Chang KA, Liao Q (2001) A single camera coupled PTV–LIF technique. Exp Fluids 31(1):63–73

Crimaldi J (1997) The effect of photobleaching and velocity fluctuations on single-point LIF measurements. Exp Fluids 23(4):325–330

Crimaldi J, Koseff J (2001) High-resolution measurements of the spatial and temporal structure of a turbulent plume. Exp Fluids 31:90–102

Fong D, Geyer W (2002) The alongshore transport of fresh water in a surface-trapped river plume. J Phys Oceanogr 32(3):957–972

Griffiths R (1986) Gravity currents in rotating systems. Annu Rev Fluid Mech 18:59–89

Griffiths R, Hopfinger E (1983) Gravity currents moving along a lateral boundary in a rotating fluid. J Fluid Mech 134:357–399

Griffiths R, Linden P (1981) The stability of buoyancy-driven coastal currents. Dyn Atmos Oceans 5(4):281–306

Horner-Devine A, Fong D, Monismith S, Maxworthy T (2006) Laboratory experiments simulating a coastal river inflow. J Fluid Mech 555:203–232

Law AK, Wang H, Herlina (2003) Combined particle image velocimetry/planar laser induced fluorescence for integral modeling of buoyant jets. J Eng Mech 129(10):1189–1196

Lentz S, Helfrich K (2002) Buoyant gravity currents along a sloping bottom in a rotating fluid. J Fluid Mech 464:251–278

Liao Q, Cowen E (2005) An efficient anti-aliasing spectral continuous window shifting technique for PIV. Exp Fluids 38(2):197–208

Lide D (2003) CRC handbook of chemistry and physics. CRC Press, Boca Raton

Lowe R, Linden P, Rottman J (2002) A laboratory study of the velocity structure in an intrusive gravity current. J Fluid Mech 456:33–48

Raffel M, Willert C, Kompenhans J (1998) Particle image velocimetry. Springer, Berlin Heidelberg New York

Stern M, Whitehead J, Hua BL (1982) The intrusion of a density current along the coast of a rotating fluid. J Fluid Mech 123:237–265

Sveen J, Cowen E (2004) Quantitative imaging techniques and their application to wavy flow. In: J G, PLF L, GK P (eds) PIV and water waves, vol 9. World Scientific, Singapore, pp 1–49

Troy C, Koseff J (2005) The generation and quantitative visualization of breaking internal waves. Exp Fluids 38:549–562

Vinger Å, McClimans T, Tryggestad S (1981) Laboratory observations of instabilities in a straight coastal current. In: The Norwegian Coastal Current, vol 2. University of Bergen, Norway, pp 553–582

Walker D (1987) A fluorescence technique for measurement of concentration in mixing liquids. J Phys E 20:217–224